Journal of Materials Chemistry A

ROYAL SOCIETY OF CHEMISTRY

PAPER

View Article Online
View Journal

Cite this: DOI: 10.1039/d6ta00970k

Size-controlled hydrothermal synthesis of crystalline high-entropy spinel oxide nanoparticles for oxygen evolution electrocatalysts

Ryoga Kato,[ab] Kazuyuki Iwase,[*b] Hiroto Okuyama,[c] Akiko Tsurumaki,[de] Hitoshi Kasai,[b] Kouki Oka,[b] Takeo Yamaguchi[c] and Takaaki Tomai[bf]

High-entropy oxides offer a promising platform for oxygen evolution reaction catalysis owing to their entropy-stabilized structures and flexible design of cation metal elements. However, conventional high-temperature synthesis leads to extensive particle growth and limits access to nanoscale particles with a higher density of catalytic sites. Here, a subcritical hydrothermal synthesis combined with catechol-assisted growth regulation is introduced to produce high-entropy single-phase spinel oxide nanoparticles with controlled crystallite sizes down to the single-nanometer scale. The resulting reduction in particle size markedly enhances the oxygen evolution activity. A linear dependence of the oxygen evolution current density on the inverse crystallite size highlights the critical role of nanoscale structures in accelerating catalytic reactions. *In situ* X-ray absorption spectroscopy reveals electronic and structural robustness of all constituent metal elements under OER conditions, with negligible shifts in the oxidation state or changes in the local coordination structure, which is distinct from the pronounced reconstruction typically observed in conventional oxide catalysts. When deployed in a membrane electrode assembly, our synthesized high-entropy oxide catalysts with the smallest particle size deliver 2.0 A cm^{-2} at 1.96 V, demonstrating practical relevance for high-current-density electrolysis. This work establishes low-temperature hydrothermal synthesis with organic molecular regulation as a powerful and scalable route to engineer highly crystalline, compositionally homogeneous high-entropy oxide nanoparticles, offering design guidelines for next-generation oxygen evolution reaction catalysts.

Received 1st February 2026
Accepted 10th May 2026

DOI: 10.1039/d6ta00970k

rsc.li/materials-a

Introduction

The oxygen evolution reaction (OER) is the anodic reaction in electrochemical water splitting. It plays a pivotal role in enabling the generation of green hydrogen using renewable electricity sources. However, the OER suffers from sluggish kinetics and a large overpotential, which significantly reduces the overall efficiency of water splitting.[1,2]

In recent years, metal oxides composed of only non-precious metal elements have drawn increasing interest as OER catalysts due to their high activity under alkaline conditions and the ability to modulate OER activity through electronic structure and structural tuning.[3–6] High-entropy oxides (HEOs), usually composed of more than five metal elements, have recently attracted significant attention as promising catalytic materials.[7–9] This growing interest is largely due to their unique electronic structure, various types of active sites formed on the surface, and high durability.[9,10] These features distinguish HEOs from traditional metal oxide catalysts, and these properties make HEOs highly attractive for various catalytic reactions, including the OER. As OER electrocatalysts, HEOs composed of transition metals have attracted considerable attention, particularly because they exhibit efficient and stable catalytic activity in alkaline solutions.[11–17]

In previous research, HEOs have typically been synthesized through a high-temperature heat treatment process (~1000 °C).[18] This synthesis process allows for the mixing of multiple metal elements at the atomic level. However, under these high-temperature conditions, the particle size tends to increase, and microsized particles are usually formed. From the viewpoint of catalysis, catalyst particles with small particle sizes are attractive due to their high surface area and a higher ratio of low-coordinated sites, which are expected to exhibit enhanced

[a]Department of Chemical Engineering, Graduate School of Engineering, Tohoku University, 6-6-11-604 Aramaki-aza Aoba, Aoba-ku, Sendai 980-8579, Japan
[b]Institute of Multidisciplinary Research for Advanced Materials, Tohoku University, 2-1-1 Katahira, Aoba-ku, Sendai, 980-8577, Japan. E-mail: kazuyuki.iwase.a6@tohoku.ac.jp
[c]Laboratory for Chemistry and Life Science, Institute of Science Tokyo, R1-17, 4259 Nagatsuta-cho, Midori-ku, Yokohama, Kanagawa, 226-8501, Japan
[d]Department of Chemistry, Sapienza University of Rome, Piazzale Aldo Moro 5 00185, Rome, Italy
[e]Hydro-Eco Research Center, Sapienza University of Rome, Via A. Scarpa 16 00161, Rome, Italy
[f]The Frontier Research Institute for Interdisciplinary Sciences, Tohoku University, 6-3 Aramaki Aoba, Aoba-ku, Sendai, Miyagi 980-0845, Japan

catalytic activity. Therefore, control over the particle size of HEOs is limited under the high-temperature conditions used during synthesis.

Supercritical and subcritical water have been widely utilized as reaction media for nanoparticle synthesis owing to their unique physicochemical properties.[19,20] In particular, the drastic changes in water properties near the supercritical state can promote the simultaneous precipitation of multiple metal species, which is expected to facilitate the formation of compositionally homogeneous multicomponent oxides. Previous studies, including our earlier work, have demonstrated that single-phase high-entropy oxides composed of five transition metals can be synthesized using supercritical water, even at relatively low temperatures around 400 °C.[21,22] Compared with supercritical water, subcritical water provides a milder reaction environment while still retaining unique properties of high-temperature and high-pressure water that promote metal oxide nucleation and crystallization.

In the present study, we employed a subcritical hydrothermal method for synthesizing size-controlled high-entropy oxide nanoparticles (HEO NPs). The physicochemical properties of water change drastically under high temperature and pressure conditions, which is expected to facilitate the formation of nanoparticles with homogeneous solid solutions at lower temperatures than those required by conventional methods. Furthermore, subcritical water can form a homogeneous phase with organic compounds, allowing organic modifiers to interact with the particle surface and suppress particle growth.[15] This milder reaction environment is particularly advantageous for the present study, as it enables effective interaction between catechol and the surface of HEO nanoparticles and precursor metal ions while minimizing thermal decomposition of the organic modifier. In this study, we propose an organic-molecule-assisted subcritical hydrothermal strategy to achieve precise particle size control of HEO NPs.

Results and discussion

The HEO NPs were synthesized using a hydrothermal method by modifying a previously reported method. Briefly, the metal-containing precursors were transferred to a Hastelloy reactor and heated at 300 °C for 60 min. Each synthesized sample was labeled according to the concentration of catechol. Samples with catechol concentrations of 0 M, 0.1 M, 0.3 M, and 0.5 M were labeled HEO-0, HEO-0.1, HEO-0.3, and HEO-0.5, respectively.

X-ray diffraction (XRD) patterns of the synthesized HEO NPs are presented in Fig. 1. The observed peaks for all HEO NPs, including the main peak around 35°, can be indexed to a cubic spinel structure with the space group $Fd\bar{3}m$ (No. 227), regardless of the catechol concentration. This result confirms that a single-phase cubic spinel oxide structure was successfully formed without any side products. This result is particularly notable, as phase separation is often observed in multicomponent systems such as HEOs.[7] An increase in catechol concentration leads to broadening of peaks, which will be discussed in detail later. Fig. S1 shows synchrotron XRD patterns of HEO NPs. This result shows good agreement with the XRD patterns in Fig. 1 and also

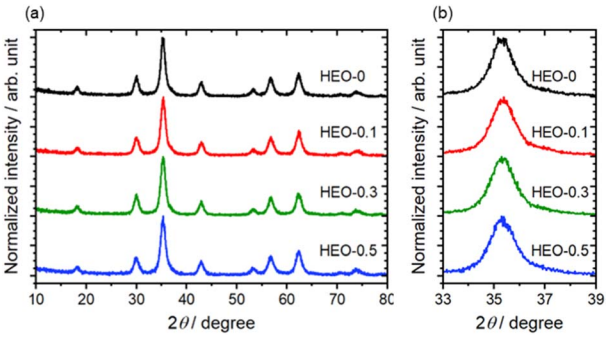

Fig. 1 XRD patterns of HEO NPs with different catechol concentrations. (a) Wide-angle view and (b) magnified view around the (311) peak.

indicates that a single phase cubic spinel oxide structure was successfully formed during the synthesis.

The particle size and morphologies of the HEO NPs are directly analyzed by transmission electron microscopy (TEM) (Fig. 2). The particle size distribution obtained from the TEM images is shown in Fig. S2. For HEO-0, particles with diameters of approximately 20 nm were observed. However, the addition of catechol significantly reduced the particle size, with nanoparticles smaller than 15 nm obtained even at low catechol concentrations. A clear trend in which increasing the catechol concentration led to progressively smaller particles was observed. Notably, the average particle diameter was approximately 5.6 nm for HEO-0.5. In addition, the particle size distribution seems to become smaller with the addition of catechol during the synthesis. Fig. S3 shows the comparison between the crystallite size calculated from the XRD pattern shown in Fig. 1 using the Halder–Wagner equation and the particle size obtained from TEM images against the concentration of catechol.[23] A similar trend was observed for both crystallite size and particle size, which decreased with increasing catechol concentration. For HEO-0.5, the calculated crystallite size was approximately 6 nm, further confirming the size reduction effect of catechol during synthesis.

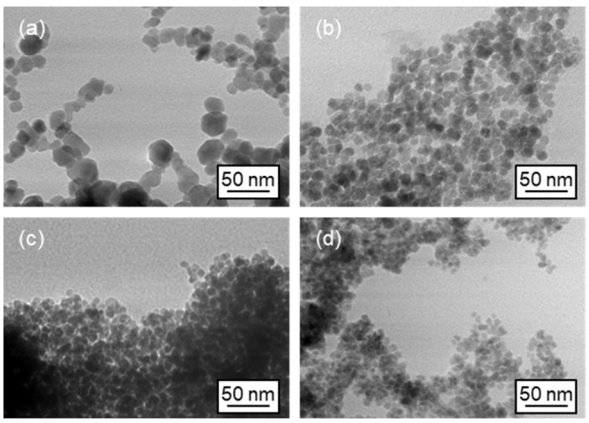

Fig. 2 TEM images of HEO NPs. (a) HEO-0, (b) HEO-0.1, (c) HEO-0.3, and (d) HEO-0.5.

In order to investigate whether catechol molecules were modified onto the surface of HEO NPs, simultaneous differential thermal analysis (DTA) and thermogravimetric analysis (TG) were conducted. Fig. S4 shows the TG and DTA curves for HEO-0.5 and HEO-0. In the TG curves, a slight weight loss was observed up to approximately 200 °C, which can be attributed to the removal of residual water.[24,25] For HEO-0.5, a significant weight loss was observed above 250 °C, which was not observed for HEO-0, accompanied by a strong exothermic peak in the DTA curve around 280–290 °C. The weight loss above 250 °C can be assigned to thermal decomposition and/or desorption of catechol. Notably, this decomposition occurs at temperatures higher than the boiling point of catechol (245 °C). This result indicates that catechol is chemically bonded to the particle surface in a stable manner.[26] These findings support that catechol molecules reduced the particle size, likely due to the suppression of crystal growth by the surface-bound catechol.

The elemental analysis by ICP-OES was conducted for HEO NPs. The elemental ratios of the starting material and HEO NPs are summarized in Fig. S5. Notably, the metal elemental ratios of HEO-0 were almost identical to those of the precursor solution; however, the ratios for HEOs synthesized with catechol are different from that of the precursor solution. Specifically, the ratio of Mn is significantly smaller compared to the precursor solution. This result indicates that catechol molecules strongly interact with Mn species. In addition, it is plausible that catechol also forms coordination complexes with other transition-metal species except Fe, resulting in partial retention of these metal ions in the solution phase during the hydrothermal process.

Further detailed structural characterization studies of the mixing state of the constituent elements were conducted by scanning transmission electron microscopy (STEM). Fig. 3 shows the HAADF-STEM images and corresponding EDX mapping of HEO-0.5. The HAADF-STEM image along the [110] zone axis is shown in Fig. 3a. In this image, the bright spots indicate the metal elements. The 16d and 8a sites of the cubic spinel structure marked with red and blue dots were clearly observed.[21] The Fourier transform (FT) image of Fig. 3a is shown in Fig. 3b. This image provides information on the crystal structure of this region. The absence of clear unassigned diffraction spots implies that HEO-0.5 has a single-phase spinel structure. These results are in good agreement with the synchrotron XRD patterns. STEM-EDX elemental mapping for the constituent metal elements (Fig. 3c–h) shows that the constituent elements are homogeneously distributed across the particles. These results indicate that no elemental segregation occurs during the synthesis, even in the presence of catechol. These results indicate that the five metal elements are uniformly distributed across the particles. The wide range STEM-EDX mapping for HEO-0.5 (Fig. S6) also revealed that no large detectable phase segregation occurred during the synthesis procedure.

Detailed analyses of the valence states and coordination environments of the metal elements were conducted using X-ray absorption spectroscopy (XAS). XAS was selected because conventional X-ray photoelectron spectroscopy (XPS) is not suitable for this system; in multicomponent oxides containing several first-row transition metals, overlapping Auger and metal 2p peaks make reliable valence analysis difficult.

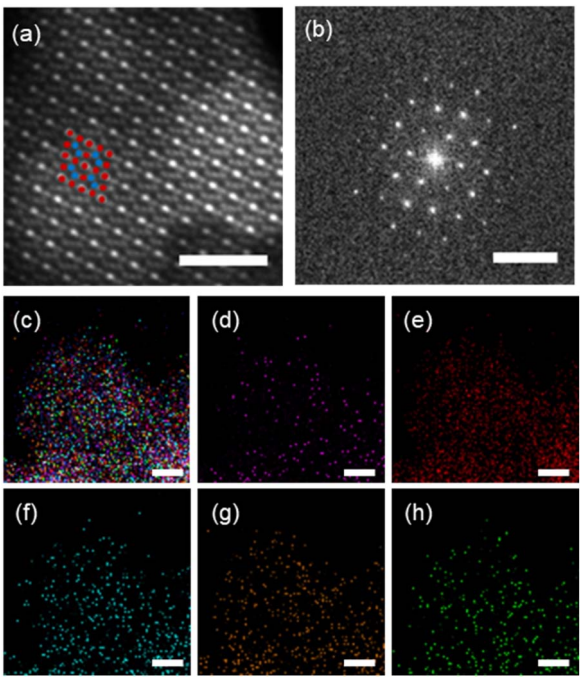

Fig. 3 STEM images of HEO NPs. (a) Magnified HAADF-STEM image (zone axis: [110]). Red and blue dots correspond to 16d sites and 8a sites of the cubic spinel structure, respectively. Scale bar: 2 nm. (b) Fourier-transformed magnified HAADF-STEM image. Scale bar: 5 nm^{-1}. (c–h) EDX-mapping of HE-SOs: (c) merged image, (d) Mn, (e) Fe, (f) Co, (g) Ni, and (h) Zn. Scale bar: 2 nm.

The XANES spectra of the Mn, Fe, Co, Ni, and Zn K-edges for HEO-0.5 are listed in Fig. 4a–e, respectively. The absorption edges of Mn, Co, Ni, and Zn exhibit absorption-edge energies similar to the corresponding metal oxides containing divalent metal ions (M(II)), whereas Fe exhibits absorption-edge energies similar to the corresponding trivalent metal ions (M(III)). These results suggest that Mn, Co, Ni and Zn exist as M(II), and Fe exists as M(III). XANES spectra of the metal K-edges for HEO-0, -0.1 and 0.3 are shown in Fig. S7. Although all metal K-edges for HEO-0.1 and HEO-0.3 exhibited a similar tendency to HEO-0.5, HEO-0 showed a different absorption-edge energy for the Mn K-edge, and the absorption edges are similar to Mn_2O_3, suggesting that Mn species for HEO-0 exist as Mn(III). This result also suggests that catechol molecules largely affect the valence state of Mn species, as discussed in the ICP analyses, whereas the particle size itself doesn't affect the valence states of the constituent metal elements.

The corresponding Fourier transformed extended X-ray absorption fine structure (FT-EXAFS) spectra also reveal well-defined first shell M–O (~1.5 Å) and second-shell M–O–M (~2.5–3.1 Å) peaks, which are observed in the cubic spinel structure (Fig. 4f–j).[27] In HEO-0.5, Ni shows clear second-shell features around ~2.6 Å, consistent with its occupancy at octahedral (16d) sites, while Zn shows clear second-shell features around ~3.1 Å, consistent with its occupancy at tetrahedral (8a)

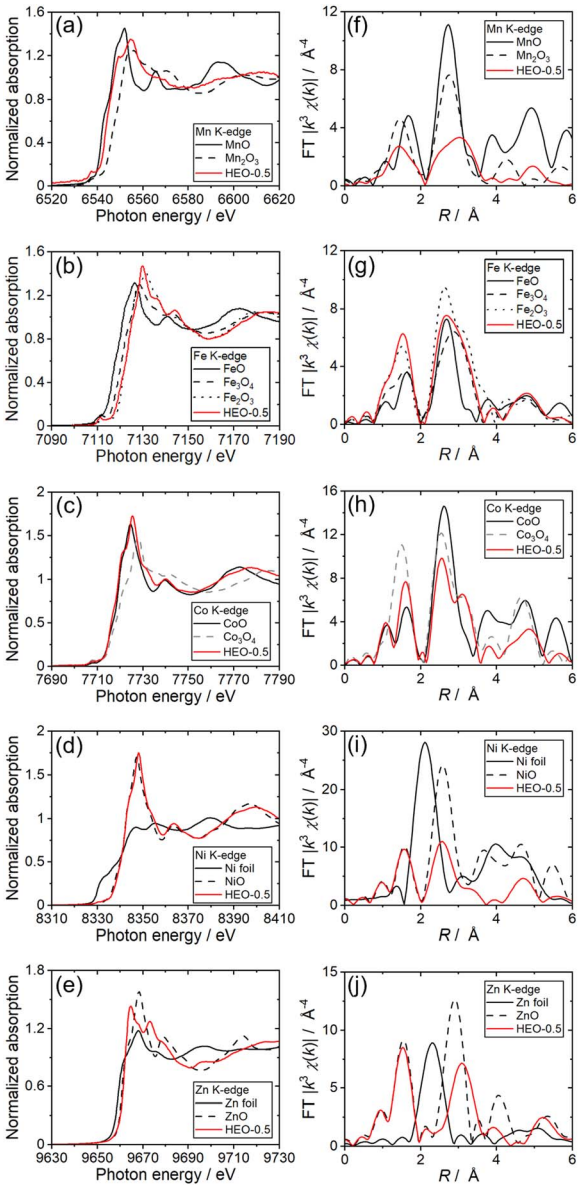

Fig. 4 Metal K-edge (a–e) XANES and (f–j) FT-EXAFS of constituent metal elements of HEO-0.5. (a and f) Mn, (b and g) Fe, (c and h) Co, (d and i) Ni, and (e and j) Zn.

sites. For the Mn, Fe, and Co K-edges, the spectra displayed features distributed over both tetrahedral (8a) and octahedral (16d) sites, suggesting that these metal elements occupy both 8a and 16d sites. FT-EXAFS spectra of the metal K-edges for HEO-0, -0.1 and 0.3 are shown in Fig. S8. The tendency is similar to that observed in the XANES spectra of these samples. Although the shapes of the FT-EXAFS spectra for HEO-0.1 and HEO-0.3 exhibited tendencies similar to that of HEO-0.5 for all metal elements, HEO-0 showed a different peak position for the Mn K-edge. The second-shell M–O–M spectra for HEO-0 showed a single peak at a shorter distance around 2.6 Å, suggesting that Mn occupies octahedral sites. These results indicate that catechol affects not only the Mn valence state but also its local coordination environment. This change is possibly the reason for the reduced Mn incorporation observed by ICP-OES, suggesting that catechol selectively modifies the Mn incorporation pathway during HEO formation.

To evaluate the OER activity, cyclic voltammetry (CV) was recorded in O_2-saturated 1 M KOH aqueous solution (Fig. 5a). All samples exhibited a clear increase in anodic current assignable to the OER approximately from 1.5–1.55 V *vs.* the reversible hydrogen electrode (RHE). A comparison among the samples clearly shows that the anodic current increases with increasing catechol concentration during the synthesis, with HEO-0.5 exhibiting the highest OER current. The current density at 1.65 V *vs.* RHE reached approximately 190 mA cm^{-2} for HEO-0.5. The overpotentials determined at a current density

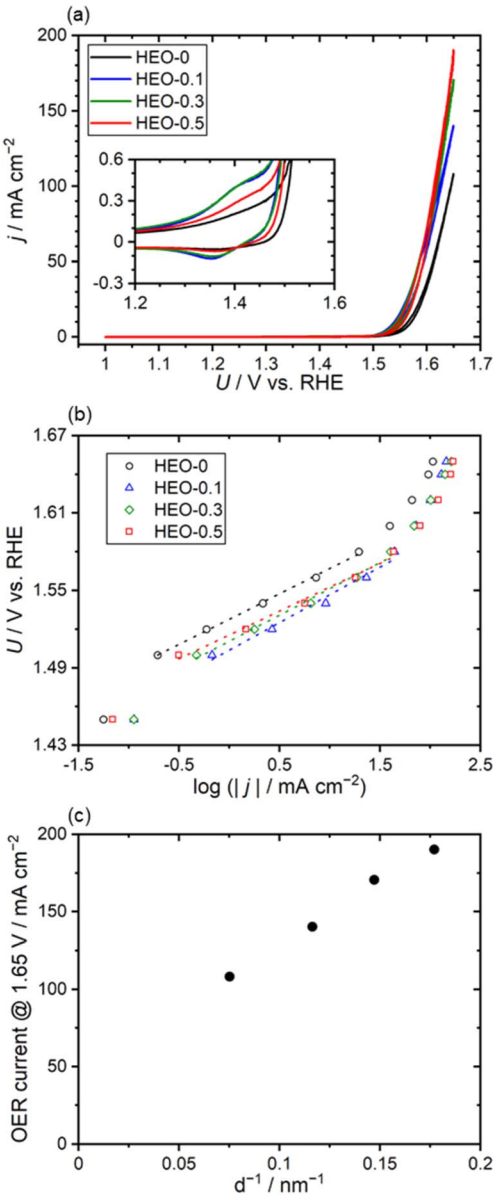

Fig. 5 OER activity of HEO NPs in this study. (a) Cyclic voltammograms of HEO NPs and (b) Tafel plots of HEO NPs obtained by the chronoamperometric measurement. (c) Summary of the current density at 1.65 V *vs.* RHE as a function of the inverse crystallite size.

of 10 mA cm^{-2} for these catalysts ranged between 342 and 327 mV, which are comparable to the values reported so far for NiFe- and CoFe-based spinel oxides, as summarized in Table S1.[28–32] HEO synthesized without catechol shows the highest overpotential, implying that catechol addition is effective for enhancing OER activity.

Fig. 5b presents the Tafel plots obtained from the chronoamperometric OER measurements. The Tafel slope value is summarized in Table S1. All HEO NPs showed linear region in the range of approximately 1.50–1.56 V and the Tafel slope value of HEO-0 was approximately 37.7 mV dec^{-1}. This value is superior to those of typical NiFe- and CoFe-based spinel oxides, as summarized in Table S1, indicating better OER kinetics of the synthesized HEO catalysts. This Tafel slope value indicates that the rate-determining step is possibly the formation of M–O species from M–OH species or M–OO- species from M–OOH species.[33] For HEO NPs synthesized using catechol, as the catechol concentration increased, the Tafel slope value slightly decreased, reaching approximately 34.0 mV dec^{-1} for HEO-0.5. Although this change does not indicate a substantial change in the overall reaction mechanism, it implies subtle modifications to the surface electronic structure and the adsorption energetics of reaction intermediates. Another possible reason is that the increase in low-coordination surface sites and lattice distortion accompanying the reduction in particle size may influence the adsorption energies of OER intermediates (*OH, *O, and *OOH), thereby affecting the reaction kinetics.[34,35]

The enhancement of OER activity could also be attributed to the reduced particle size caused by increasing catechol concentration upon catechol addition. Therefore, to clarify the correlation between OER activity and particle size, the current density at 1.65 V *vs.* RHE was plotted as a function of the inverse crystallite size ($1/d$), as shown in Fig. 5c. A clear linear relationship was observed against the inverse crystallite size, demonstrating that the reduction in particle size directly contributes to the enhancement of OER current density. This trend suggests that the increased number of accessible active sites, together with the higher density of low-coordination atoms and surface lattice distortion, plays a significant role in accelerating the OER. In particular, previous studies have reported that surface strain originating from the configurational disorder of constituent elements can act as active sites of the reaction, especially in nanoscale high-entropy oxides.[36] The present results for our HEO catalysts indicate that not only the metal mixing entropy effect suggested by previous studies but also the particle size showed a positive effect on the catalytic activity. Overall, these findings demonstrate that particle-size control through organic molecule modification not only tunes the geometric structure of the catalyst but also leads to substantial improvements in electrocatalytic activity.

To investigate whether the electrochemical surface area (ECSA) supports the observed particle-size-dependent OER activity, the double-layer capacitance (C_{dl}) was estimated from CVs recorded in the non-faradaic region at different scan rates (Fig. S9). In this study, carbon nanotubes (CNTs) were added during the preparation of HEO-modified electrodes (see the Experimental section for details). However, CNT-free HEO electrodes were specifically employed for the C_{dl} measurements to exclude the contribution of CNT capacitance. The estimated C_{dl} did not show a monotonic increase with decreasing particle size, nor did it correlate with the trend in OER activity. This result indicates that CV-derived C_{dl} is not a reliable descriptor of the ECSA of HEO-modified electrodes under the present electrode configuration, likely due to its sensitivity to film conductivity, interparticle contact, and electrolyte accessibility. Since the capacitance in CNT-containing electrodes is dominated by CNTs, the C_{dl}-derived ECSA was not used as a quantitative measure of active site density in this study.

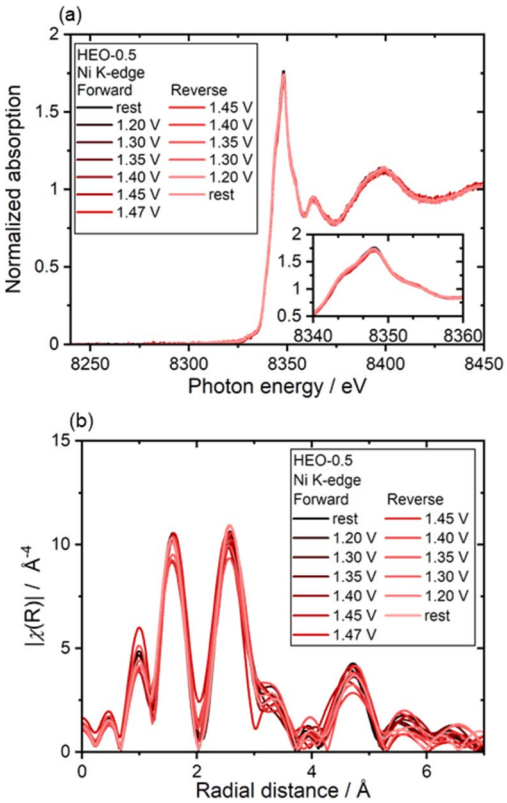

Fig. 6 *In situ* (a) XANES and (b) FT-EXAFS spectra of the Ni K-edge for HEO-0.5 in the redox region. The potential sweep was initially performed from 1.2 V to 1.47 V in the forward scan and then returned to 1.2 V during the reverse scan.

To investigate the redox behavior and local coordination structure changes of the constituent elements of the redox region (around 1.4 V, as shown in Fig. 5a) and around the starting potential of the OER, *in situ* XAFS measurements were conducted for the HEO with the highest OER activity, HEO-0.5 (Fig. 6). Previous studies have suggested that nanoparticles with particle sizes below approximately 20 nm possess a higher ratio of surface metal atoms, making it possible to analyze redox and structural changes.[37–39]

Fig. 6a and b show the *in situ* XANES and FT-EXAFS spectra for the Ni K-edge, respectively. For the XANES spectra, no significant energy shifts or noticeable changes in white-line intensity were observed within the redox potential window of 1.2–1.47 V *vs.* RHE. This behavior contrasts with the pronounced structural changes previously observed for

monometallic Ni-based oxides and is instead consistent with the behavior reported for HEOs with particle sizes around 20 nm composed of Mn, Fe, Co, Ni and Zn.[37] This result realized the moderate oxidation and structural stability of Ni species. In addition, no obvious changes for the M–O peaks or M–O–M peaks were observed for *in situ* FT-EXAFS (Fig. 6b). These results also indicate that HEOs possess structural stability against potential changes within the potential region examined in this study. *In situ* XANES and FT-EXAFS spectra for other elements are summarized in Fig. S10 and S11, respectively. For all metal species, no significant energy shifts or noticeable changes in white-line intensity were observed within the redox potential window of 1.2–1.47 V in XANES spectra and FT-EXAFS. These results also suggest that all constituent elements in HEO-0.5 show structural stability within the potential window examined in this study.

It is well known that transition-metal oxides, including Ni-, Co-, and Fe-containing spinel oxides, often undergo structural reconstruction during the OER, involving phase transitions (*e.g.*, from spinel oxides to layered metal oxyhydroxide structures) and changes in the oxidation state.[39,40] These reconstruction processes are widely considered to play a key role in enhancing the OER activity of transition-metal oxides.[41] In contrast to conventional spinel-type transition metal oxides, which typically undergo irreversible surface reconstruction into hydroxide or oxyhydroxide phases under OER conditions,[42,43] HEO-0.5 retains a relatively stable multi-cation local structure even under applied potential conditions, as evidenced by *in situ* XAS analysis. This relatively higher structural stability, while not excluding subtle structural modifications at the outermost surface, can be rationalized by the synergistic effects of entropy-driven stabilization and the high crystallinity of the nanoparticles. First, the homogeneous mixing of multiple metal cations gives rise to higher configurational entropy, which can contribute to the stabilization of the multication spinel framework. This stabilization may mitigate cation segregation and extensive structural reconstruction, both of which are closely related to degradation in conventional spinel oxide catalysts.[43,44] Second, unlike typical amorphous or polycrystalline catalysts, where phase transformations often initiate at grain boundaries or defect sites,[45] the high crystallinity of the single-nanometer scale HEO-0.5 nanoparticles could provide a robust framework that resists extensive self-oxidation and bulk phase transformation.[45] The low density of extended defects in highly crystalline HEO-0.5 may also inhibit the nucleation of oxyhydroxide phases. Thus, while subtle surface reconstruction or trace metal dissolution cannot be excluded, the *in situ* XAS results indicate that HEO-0.5 largely preserves its multication spinel framework under the examined oxidative conditions.

To quantitatively evaluate the changes in the oxidation state for each metal species, the mid-point energies (half-height positions of the absorption edge) of the *in situ* XANES spectra were plotted as a function of the applied potential (Fig. 7).[38] For Ni, a reversible shift toward higher energies was observed, particularly in the high-potential region above 1.45 V. In contrast, Mn, Fe and Zn exhibited no apparent potential-dependent energy shifts within the range of 1.2–1.47 V. The

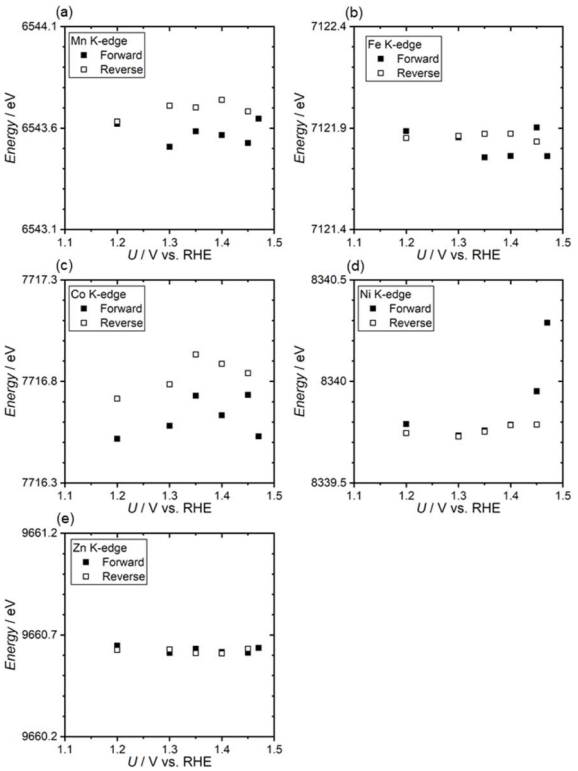

Fig. 7 Mid-point plots of the *in situ* XANES spectra for the metal K-edges. (a) Mn, (b) Fe, (c) Co, (d) Ni, and (e) Zn.

Co K-edge appears to slightly shift to a higher energy region under higher applied potentials, although the noise by the fluctuation was observed. This indicates that, over the potential window where the redox process proceeds, as shown in Fig. 5a, the average oxidation states of these metals, Mn, Fe and Zn, remain essentially unchanged or undergo only minimal changes. On the other hand, Co and Ni show moderate redox activity during the potential applications. These observations are consistent with the absence of obvious potential-dependent features in the full XANES spectra shown in Fig. 6, S9 and S10, further supporting that the constituent elements in HEO-0.5 remained more stable under reaction conditions. This suggests that entropy-driven stabilization by multi-metal cation mixing and the robust spinel framework of the high-entropy oxide suppress local structural changes, leading to enhanced electronic stability relative to traditional oxide catalysts.[28–32]

For further investigating the impact of the synthesis process on morphology and OER activity, HEOs were synthesized under hydrothermal conditions at 200 °C with and without catechol, which are labelled as HT-HEO-0.5 and HT-HEO-0, respectively. In the XRD patterns of both catalysts (Fig. S12), clear peaks assignable to a single phase spinel structure were observed, as for HEO-0–HEO-0.5, although main peaks around 36° were broadened for HT-HEO-0.5. TEM images also show that nanoscale particles were obtained (Fig. S13). However, amorphous-like regions appearing with brighter contrast were also observed along with darker contrast particles, which could originate from more crystalized particles. OER activities were

evaluated in a similar manner to those of the HEO catalysts (Fig. S14). Clear OER current is observed for both catalysts (Fig. S14a). Notably, the overpotential for HT-HEO-0.5 shows the smallest value among the samples synthesized in this study. However, the Tafel plot for HT-HEO-0.5 shows a larger slope value than those of the other samples synthesized in this study (Fig. S14b). The Tafel slope value for HT-HEO-0.5 also shows the largest value, as summarized in Table S1. The OER current of the samples against the inverse of crystalline size is plotted in Fig. S14c. Interestingly, the OER current at 1.65 V for HT-HEO catalysts shows the same tendency as the HEO catalysts, where catalysts with smaller crystalline sizes show higher OER current. However, although the crystallite sizes are similar to HEO catalysts, the OER current at 1.65 V for HT-HEO shows a smaller value. This result indicates that synthesis process can affect the OER activity. We hypothesize that the superior OER activity for HEO catalysts is derived from higher crystallinity due to the higher temperature during the synthesis. Further study investigating the relationship between the physicochemical properties, such as crystallinity and size, and OER activity is ongoing in our laboratory.

To evaluate the practical applicability of the synthesized HEO, we integrated the most OER-active composition, HEO-0.5, into a MEA and tested its performance under device-relevant conditions. Anion exchange membrane water electrolysis (AEMWE) cells were assembled using HEO-0.5 as the anodic OER catalyst and PtRu/C as the cathode, operated with a commercially available thin anion-exchange membrane and 1.0 M KOH at 80 °C. The anodic catalyst layer composition was systematically tuned by varying the mass ratio of HEO-0.5 to metallic Ni while keeping the total loading weight constant. Fig. S15a shows the polarization curves obtained from these MEAs. The dependence of MEA performance on the Ni : HEO ratio highlights the importance of balancing electronic conductivity and active site density in the anodic catalyst layer. At a Ni : HEO ratio of 5 : 5, the polarization curve was shifted to lower cell voltages across the entire current density range compared with those at 3 : 7 and 7 : 3, indicating that this composition provided the most efficient compromise between a well-percolated conductive network and a high density of active HEO-0.5 sites. When the Ni fraction was reduced to 30 wt% (Ni : HEO = 3 : 7), the cell voltage slightly increased, which is attributed to higher ohmic and contact resistances associated with an insufficiently connected Ni network. Conversely, when the Ni fraction is increased to 70 wt% (Ni : HEO = 7 : 3), the performance deteriorates more significantly, especially in the high-current-density region, indicating that the loss of active HEO-0.5 per geometric area outweighs the benefit of enhanced conductivity. These trends indicate that performance is governed by the balance between electronic conductivity and active-site density, and that an intermediate Ni content maximizes the effective utilization of both the conductive additive and the catalyst.

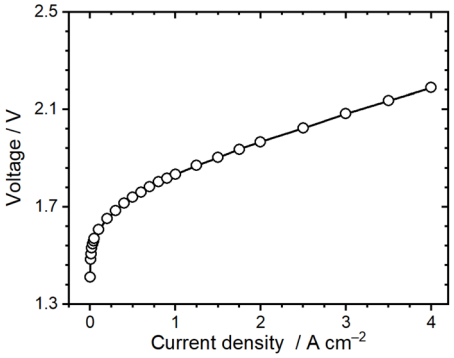

Fig. 8 Polarization curve of the AEMWE cell using HEO-0.5/Ni anodes in 1.0 M KOH at 80 °C. In this measurement, the HEO-0.5 : Ni ratio is 5 : 5. For details of the optimization of the catalyst : Ni ratio, see SI Fig. S15.

Fig. 8 shows the polarization curve obtained from the MEA with the optimized Ni : HEO-0.5 ratio (5 : 5). The cell with an optimized Ni : HEO ratio of 5 : 5 exhibited a current density of 1.0 A cm^{-2} at 1.83 V and reached 4.0 A cm^{-2} at 2.19 V under differential-pressure-free conditions. These results demonstrate that the fully non-noble HEO-0.5 catalyst can drive the OER in a device-relevant configuration, achieving high current densities at low cell voltages around 1.8–2.2 V. When compared with recently reported non-noble AEMWE cells operated at 80 °C in 1.0 M KOH, which typically require 1.65–2.03 V to deliver 1.0 A cm^{-2}, the present HEO-0.5 MEA lies in the upper tier of performance (Table S2 and Fig. S16),[46–53] despite the relatively modest catalyst loading and the absence of advanced electrode structuring. This device-level activity is in good agreement with the high intrinsic OER activity of HEO-0.5 evidenced by half-cell measurements (Table S2 and Fig. S16).

To gain further insight into the origin of these MEA-level trends, electrochemical impedance spectroscopy (EIS) was conducted under operating conditions (Fig. S15b, see the Experimental section for experimental details). In all cases, the high-frequency intercept of the Nyquist plots was nearly identical, indicating that the bulk ohmic resistance of the membrane and cell hardware was essentially unchanged by the Ni : HEO ratio. In contrast, the diameter of the main semicircle, associated with the charge-transfer resistance (R_{ct}), depended strongly on the anode composition: R_{ct} remained small for Ni : HEO = 3 : 7 and 5 : 5 but increased markedly for 7 : 3, in line with the larger voltage losses observed for the Ni-rich electrode at high current densities. Furthermore, EIS-based analysis of the cell voltage allowed separation of the anodic and cathodic contributions at each electrode (Fig. S15c and d). The cathodic overpotential was almost identical for all cells, as expected from the identical cathode configuration, whereas the anodic overpotential varied with the Ni : HEO ratio and reached a minimum at 5 : 5. This composition-dependent trend in anodic overpotential closely matches the polarization behavior in Fig. 8, with the lowest anodic losses coinciding with the best MEA performance at Ni : HEO = 5 : 5.

Overall, the combination of polarization and EIS analyses demonstrates that the size-controlled HEO-0.5 catalyst, when combined with an optimally balanced Ni content in the anode, delivers high MEA performance using only non-noble metals. Because the catalyst is entirely non-noble, increasing its loading and refining the electrode architecture should further enhance

MEA performance. Since the choice of metal cations and cell configuration can influence both the catalytic activity and the stability of the catalyst[14] and MEA cell operation, further studies aimed at enhancing stability as well as OER activity represent promising future directions.

Conclusions

In conclusion, in this study, we have demonstrated a subcritical hydrothermal synthesis strategy combined with surface organic modification as an effective route to synthesize size-controlled multi-metal HEOs as OER catalysts. This approach enabled the synthesis of single-phase, highly crystalline cubic spinel HEO nanoparticles with tunable particle sizes down to the single-nanometer scale, which is difficult to achieve *via* conventional high-temperature annealing synthesis protocols. Systematic particle size reduction induced by catechol addition resulted in a pronounced enhancement of OER activity. The optimized HEO-0.5 catalyst delivered high current densities and exhibited a clear linear correlation between the OER current density and the inverse crystallite size, highlighting the critical role of nanoscale structural control in maximizing accessible active sites. Beyond activity enhancement, *in situ* XAS analysis revealed that the multi-cation local structure of HEO-0.5 remains relatively stable under potential applied conditions, showing minimal changes in the oxidation state and coordination environment. This behavior contrasts sharply with the extensive surface reconstruction typically observed in conventional oxide catalysts and can be attributed to the synergistic effects of entropy-driven structural stabilization and high crystallinity enabled by the subcritical hydrothermal synthesis process. Furthermore, the practical relevance of this material design was demonstrated by MEA measurements, where the HEO-0.5 catalyst achieved high current densities at low cell voltages. Taken together, this work establishes subcritical hydrothermal synthesis with organic molecular regulation as a powerful and scalable platform for designing durable, high-performance HEO catalysts, providing valuable guidelines for OER catalysts in practical water electrolysis systems.

Experimental section

Material synthesis

HEO NPs were synthesized *via* subcritical hydrothermal processing. A mixture of 0.111 mmol manganese(II) acetate tetrahydrate (Wako, Guaranteed Reagent grade, 99.9%), 0.222 mmol iron(II) acetate (Sigma-Aldrich, 99.99%), 0.056 mmol cobalt(II) acetate tetrahydrate (Wako, Guaranteed Reagent grade, >99.0%), 0.056 mmol nickel(II) acetate tetrahydrate (Kanto Chemical, 98.0%), and 0.056 mmol zinc(II) acetate dihydrate (Wako, Guaranteed Reagent grade, >99.9%) was dissolved in 5 mL of ultrapure water (Milli-Q EQ 7000, 18.2 MΩ cm^{-1}). The resulting solution, along with a predetermined amount of catechol (Wako, Guaranteed Reagent grade), was sealed in a 10 mL Hastelloy tube reactor. The reactor was heated at 300 °C for 60 minutes, and after cooling, the contents were transferred to a centrifuge tube. The product was washed several times with ultrapure water, and unreacted precursors were removed by repeated centrifugation. The collected particles were then redispersed in water and freeze-dried to obtain the final powder samples.

Physical characterization

The crystal structure of the synthesized HEO NPs was characterized by powder X-ray diffraction (XRD) using a SmartLab 9MTP diffractometer (Rigaku) with Cu-Kα radiation ($\lambda = 1.5418$ Å). Diffraction patterns were recorded over a 2θ range of 10° to 80° at a scan rate of 3.00° min^{-1}. The step size was set to 0.02°, with an accelerating voltage of 45 kV and a tube current of 200 mA. The primary particles of the synthesized HEO NPs were examined using transmission electron microscopy (TEM, HITACHI H-7650) operated at an accelerating voltage of 100 kV and a filament current of 20 mA.

The amount of organic modifier bound to the product was evaluated by thermogravimetry differential thermal analysis (TG-DTA, Thermo plus EvoII (Rigaku)). The sample was heated from room temperature to 800 °C at a rate of 10 °C min^{-1} under a flow of pure air at 100 mL min^{-1}. Prior to measurement, the samples were preheated at 60 °C for at least one hour to remove moisture contained within the particles. The elemental ratio of HEO NPs was analyzed by inductively coupled plasma atomic emission spectroscopy (ICP-AES) using SPECTRO ARCOS (SPECTRO Analytical Instruments, Germany). Scanning transmission electron microscopy (STEM) observations were performed using a Titan3 60–300 Double Corrector microscope (FEI Company) equipped with a Super-X system operated at 200 kV. X-ray absorption spectroscopy (XAS) measurements were carried out at the BL01B1 and BL14B2 beamlines of SPring-8 (Japan Synchrotron Radiation Research Institute (JASRI)). A Si(111) double-crystal monochromator was employed for energy selection. The *ex situ* XAS measurements were performed in transmission mode, while the *in situ* measurements were conducted in fluorescence mode using a 19-element solid-state detector. The obtained data were analyzed using ATHENA software.[54] The energy levels were calibrated by setting the first peak maximum in the Cu foil spectrum equal to 8980.3 eV during the measurements.

Electrochemical measurements

Electrochemical measurements were conducted in a custom-built PTFE electrochemical cell containing 70 mL of 1 M potassium hydroxide (KOH) aqueous solutions as the electrolyte. During measurements, the electrolyte was continuously saturated with oxygen (O_2) by bubbling O_2 gas through the solution. A three-electrode setup was employed, consisting of the catalyst-modified glassy carbon working electrode, a Hg/HgO (1 M NaOH) reference electrode, and a graphite rod as the counter electrode, respectively. The working electrodes were prepared by drop-casting a catalyst ink onto a glassy carbon electrode, which was polished using an alumina slurry prior to use. The catalyst ink was prepared by dispersing 3 mg of the synthesized catalyst and 2 mg of oxidized carbon nanotubes (Sigma-Aldrich) in a mixture of 40 μL Nafion solution (5 wt%, Sigma), 200 μL isopropanol (Wako), and 400 μL ultrapure water.

The suspension was first vortexed and then sonicated for 20 minutes to achieve a homogeneous dispersion. A volume of 7.5 μL of the ink was drop-cast onto a 5 mm-diameter glassy carbon electrode and dried at room temperature. The working electrode was rotated at 900 rpm using a rotating electrode system (Pine Research Instrumentation). All electrochemical measurements were performed using a potentiostat (SP-150e, Bio-Logic).

Preparation of the membrane electrode assembly

The water electrolysis performance of the synthesized catalysts in this study was also investigated by the membrane electrode assembly (MEA) following the reported method.[55,56] $Pt_{32}Ru_{16}$/C (Tanaka Precious Metal Technologies) was used as the cathode catalyst in the MEA. PiperION-A (13.3 mg, Versogen) was dissolved in a mixed solvent consisting of ethanol (3.5 mL) and deionized water (1.5 mL), and the solution was stirred overnight at 20 °C. Subsequently, 40 mg of $Pt_{32}Ru_{16}$/C was added to the ionomer solution and thoroughly mixed in a planetary ball mill (Pulverisette 6, Fritsch) for 1 h at 150 rpm using 5 mm ZrO_2 balls. The resulting catalyst ink was sprayed onto a PiperION anion-exchange membrane (20 μm thickness, Versogen) using a spray coater (Nordson K.K.) to form a cathode catalyst layer with a geometric area of 1 cm^2 and a Pt loading of 0.3 mgPt cm^{-2}.

To prepare the anode catalyst ink, a total of 40 mg of a physical mixture of HEO-0.5 and Ni particles (Aldrich, <100 nm) was combined with PiperION-A (13.3 mg), deionized water (1.5 mL), and ethanol (3.5 mL). The mass ratio of Ni to HEO was adjusted as described in the main text, while keeping the total mass of Ni and HEO constant at 40 mg. The suspension was mixed in a planetary ball mill under the same conditions as for the cathode ink (1 h, 150 rpm, 5 mm ZrO_2 balls), and then sprayed onto the opposite side of the PiperION membrane to form the anode catalyst layer. The anode loading was controlled so that the combined mass of Ni and HEO was 1.2 mg cm^{-2}. Specially designed electrolyzer cell hardware (Chemix, Japan) was used for all water electrolysis tests, and the MEA was sealed between the bipolar plates with gaskets of appropriate thickness prior to measurements.

Water electrolysis test

A 1 M KOH solution was circulated through the electrolyzer at a flow rate of 5 mL min^{-1} overnight to activate the membrane and ionomer by exchanging Cl^- with OH^-. Electrochemical impedance spectroscopy (EIS) was monitored at a cell voltage of 1.5 V using an impedance analyzer (Solartron 1260) coupled with an electrochemical interface (Solartron 1287) until stable spectra were obtained. The cell temperature was then increased to 80 °C. To maintain the operating temperature, KOH solutions preheated to 80 °C were supplied to the anode and cathode through heated tubing. After stable impedance spectra were confirmed at 80 °C, the MEA was conditioned by applying a current density of 0.2 A cm^{-2} for 20 min. Polarization curves were then recorded to evaluate the water electrolysis performance. During all measurements, the alkaline electrolyte was continuously circulated on both the anode and cathode sides. Electrolysis tests were carried out using a charge–discharge system (Hokuto Denko Co., Ltd).

Electrode-resolved EIS measurements in water electrolyzers were performed using a dual-reference-electrode electrolyzer cell based on the design reported by Nagasawa *et al.*[57] The cell allows reference electrodes to be inserted on both the anode and cathode sides of the membrane, enabling separation of the local anodic and cathodic potential responses. Before the measurement, the reference-electrode compartments were filled with 1 M KOH and allowed to stabilize for approximately 20 min. Mini-HydroFlex reference electrodes were then inserted into both sides of the cell. EIS spectra were recorded using a Solartron 1260 impedance analyzer coupled with a Solartron 1287 electrochemical interface. The anodic and cathodic impedance contributions were evaluated from the AC potential responses between each electrode and the corresponding nearby reference electrode.

Author contributions

R. K. performed the synthesis, structural analysis, and electrochemical measurements, participated in data analysis, and contributed to the initial draft of the manuscript. K. I. conceived and designed the study, supervised the project, analysed the data, and wrote the initial draft of the manuscript. A. T., K. O., and H. K. conducted synchrotron XRD measurements at the NanoTerasu facility. H. O. and T. Y. provided discussion on the interpretation of OER activity, performed the MEA tests, contributed to data interpretation, and wrote the MEA-related sections of the manuscript. T. T. contributed to experimental planning and provided project supervision. All authors discussed the results and contributed to the final version of the manuscript.

Conflicts of interest

The authors declare no conflict of interest.

Data availability

The data supporting this article have been included as part of the supplementary information (SI). Supplementary information is available. See DOI: https://doi.org/10.1039/d6ta00970k.

Acknowledgements

This work was supported by "Crossover Alliance to Create the Future with People, Intelligence and Materials" from MEXT, Japan. K. I. acknowledges financial support from the JSPS KAKENHI Grant (22H02175 and 23KK0103), the JST PRESTO program (JPMJPR2371), and the Kato Foundation for Promotion of Science (KJ-3305), the Nippon Sheet Glass Foundation for Materials Science and Engineering, the JGC-S Scholarship Foundation (No. 2301) and the Iwatani Naoji Foundation. This work was also supported by the Material Solutions Center (MaSC), Tohoku University and the Central Analytical Facility, IMRAM, Tohoku University, Japan. Synchrotron radiation

experiments were performed using the BL01B1 and BL14B2 beamlines of SPring-8 (Proposal No. 2025B1740, 2025A1811, 2024B1682, 2024B209, 2024A1587, 2023B1670, and 2023B2081). We also acknowledge Dr. Y. Hayasaka at Tohoku University for the HRTEM observations. The authors also thank the Nano-Terasu Synchrotron Light Source, the Tohoku University NanoTerasu International Co-creation Utilization Promotion Support System to access their synchrotron facility within the research collaboration entitled "Post-mortem XPS and *in situ* XRD analyses of cathode-electrolyte interphase stabilized by ionic liquids". The authors acknowledge Prof. Yuuki Sugawara at the Institute of Science Tokyo for his fruitful discussion.

References

1 Y. Matsumoto and E. Sato, *Mater. Chem. Phys.*, 1986, **14**, 397–426.
2 Y. Sugawara, K. Iwase, R. Iimura, T. Yabu, A. Nasu, M. Matsui, I. Honma, T. Yamaguchi and H. Kobayashi, *ACS Appl. Mater. Interfaces*, 2025, **17**, 22487–22497.
3 Y. Yan, B. Y. Xia, B. Zhao and X. Wang, *J. Mater. Chem. A*, 2016, **4**, 17587–17603.
4 D. U. Lee, P. Xu, Z. P. Cano, A. G. Kashkooli, M. G. Park and Z. Chen, *J. Mater. Chem. A*, 2016, **4**, 7107–7134.
5 T. Katsumata, S. Kobata, Y. Watase, R. Aso, S. Yagi, Y. Kimura, K. Amezawa and T. Nakamura, *ACS Appl. Nano Mater.*, 2025, **8**, 21215–21223.
6 Y. Sugawara and T. Yamaguchi, *Chem. Rec.*, 2025, **25**, e202400246.
7 M.-H. Tsai and J.-W. Yeh, *Mater. Res. Lett.*, 2014, **2**, 107–123.
8 Z. Shi, L. Wang, Y. Huang, X. Y. Kong and L. Ye, *Mater. Chem. Front.*, 2024, **8**, 179–191.
9 Y. Sun and S. Dai, *Sci. Adv.*, 2021, **7**, eabg1600.
10 K. Mori, N. Hashimoto, N. Kamiuchi, H. Yoshida, H. Kobayashi and H. Yamashita, *Nat. Commun.*, 2021, **12**, 3884.
11 M. Vedanarayanan, C. Pitchai and C.-M. Chen, *J. Mater. Chem. A*, 2025, **13**, 18040–18061.
12 X. Zhang, X. Wang and X. Lv, *ChemSusChem*, 2025, **18**, e202401663.
13 J. Wang, J. Zhang, H. Yu, L. Chen, H. Jiang and C. Li, *ACS Mater. Lett.*, 2024, **6**, 1739–1745.
14 M. Rafique, T. Yao, S. Ma, Y. Xu, L. Li, J. Han, Q. Fu, W. Li, Z. Yuan, K. Wang and B. Song, *Adv. Funct. Mater.*, 2025, **36**, e12495.
15 Z. Sun, Y. Zhao, C. Sun, Q. Ni, C. Wang and H. Jin, *Chem. Eng. J.*, 2022, **431**, 133448.
16 Y. Wang, H. Liu, J. Chen, K. Han, T. Xia, H. Yang, X. Yuan and Y. Zhao, *J. Power Sources*, 2025, **655**, 237936.
17 H. Liu, Y. Wang, J. Chen, X. Yi, H. Yang, X. Yuan and Y. Zhao, *J. Power Sources*, 2025, **632**, 236402.
18 Z. Lun, B. Ouyang, D. H. Kwon, Y. Ha, E. E. Foley, T. Y. Huang, Z. Cai, H. Kim, M. Balasubramanian, Y. Sun, J. Huang, Y. Tian, H. Kim, B. D. McCloskey, W. Yang, R. J. Clement, H. Ji and G. Ceder, *Nat. Mater.*, 2021, **20**, 214–221.
19 T. Adschiri, S. Takami, M. Umetsu, S. Ohara, T. Naka, K. Minami, D. Hojo, T. Togashi, T. Arita, M. Taguchi, M. Itoh, N. Aoki, G. Seong, T. Tomai and A. Yoko, *Bull. Chem. Soc. Jpn.*, 2023, **96**, 133–147.
20 A. Yoko, T. Kamonvarapitak, G. Seong, T. Tomai and T. Adschiri, *ChemNanoMat*, 2022, **8**, e202100495.
21 K. Iwase and I. Honma, *ACS Appl. Energy Mater.*, 2022, **5**, 9292–9296.
22 S. Hanabata, K. Kusada, T. Yamamoto, T. Toriyama, S. Matsumura, S. Kawaguchi, Y. Kubota, Y. Nishida, M. Haneda and H. Kitagawa, *J. Am. Chem. Soc.*, 2024, **146**, 181–186.
23 A. Yoko, H. Naito, G. Seong, T. Tomai and T. Adschiri, *J. Phys. Chem. C*, 2021, **125**, 19489–19496.
24 J. J. Calvin, P. F. Rosen, N. L. Ross, A. Navrotsky and B. F. Woodfield, *J. Mater. Res.*, 2019, **34**, 416–427.
25 F. Kunc, M. Gallerneault, O. Kodra, A. Brinkmann, G. P. Lopinski and L. J. Johnston, *Anal. Bioanal. Chem.*, 2022, **414**, 4409–4425.
26 Y. Omura, A. Yoko, G. Seong, T. Tomai and T. Adschiri, *CrystEngComm*, 2021, **23**, 5353–5361.
27 M. H. Nilsen, C. Nordhei, A. L. Ramstad, D. G. Nicholson, M. Poliakoff and A. Cabañas, *J. Phys. Chem. C*, 2007, **111**, 6252–6262.
28 H. Zhong, T. Liu, S. Zhang, D. Li, P. Tang, N. Alonso-Vante and Y. Feng, *J. Energy Chem.*, 2019, **33**, 130–137.
29 W. Xu, F. Lyu, Y. Bai, A. Gao, J. Feng, Z. Cai and Y. Yin, *Nano Energy*, 2018, **43**, 110–116.
30 X. Chen, Z. Yan, M. Yu, H. Sun, F. Liu, Q. Zhang, F. Cheng and J. Chen, *J. Mater. Chem. A*, 2019, **7**, 24868–24876.
31 Y. Wang, T. Zhou, K. Jiang, P. Da, Z. Peng, J. Tang, B. Kong, W. B. Cai, Z. Yang and G. Zheng, *Adv. Energy Mater.*, 2014, **4**, 1400696.
32 S. Mao, Z. Wen, T. Huang, Y. Hou and J. Chen, *Energy Environ. Sci.*, 2014, **7**, 609–616.
33 T. Shinagawa, A. T. Garcia-Esparza and K. Takanabe, *Sci. Rep.*, 2015, **5**, 13801.
34 J. Rossmeisl, Z. W. Qu, H. Zhu, G. J. Kroes, J. K. Nørskov and J. Electroanall, *Chem*, 2007, **607**, 83–89.
35 I. C. Man, H.-Y. Su, F. Calle-Vallejo, H. A. Hansen, J. I. Martínez, N. G. Inoglu, J. Kitchin, T. F. Jaramillo, J. K. Nørskov and J. Rossmeisl, *ChemCatChem*, 2011, **3**, 1159–1165.
36 R. R. Rao, A. Bucci, S. Corby, B. Moss, C. Liang, A. Gopakumar, I. E. L. Stephens, J. Lloret-Fillol and J. R. Durrant, *ACS Catal.*, 2024, **14**, 11389–11399.
37 K. Iwase, I. Honma and T. Tomai, *ACS Catal.*, 2026, **16**, 7395–7403.
38 B. J. Kim, E. Fabbri, D. F. Abbott, X. Cheng, A. H. Clark, M. Nachtegaal, M. Borlaf, I. E. Castelli, T. Graule and T. J. Schmidt, *J. Am. Chem. Soc.*, 2019, **141**, 5231–5240.
39 E. Fabbri, M. Nachtegaal, T. Binninger, X. Cheng, B. J. Kim, J. Durst, F. Bozza, T. Graule, R. Schaublin, L. Wiles, M. Pertoso, N. Danilovic, K. E. Ayers and T. J. Schmidt, *Nat. Mater.*, 2017, **16**, 925–931.
40 D. Friebel, M. W. Louie, M. Bajdich, K. E. Sanwald, Y. Cai, A. M. Wise, M. J. Cheng, D. Sokaras, T. C. Weng,

R. Alonso-Mori, R. C. Davis, J. R. Bargar, J. K. Norskov, A. Nilsson and A. T. Bell, *J. Am. Chem. Soc.*, 2015, **137**, 1305–1313.
41 B. Sarac and A. Sezai Sarac, *ChemCatChem*, 2024, **16**, e202400022.
42 H. Ding, H. Liu, W. Chu, C. Wu and Y. Xie, *Chem. Rev.*, 2021, **121**, 13174–13212.
43 M. S. Burke, L. J. Enman, A. S. Batchellor, S. Zou and S. W. Boettcher, *Chem. Mater.*, 2015, **27**, 7549–7558.
44 S. Samira, J. Hong, J. C. A. Camayang, K. Sun, A. S. Hoffman, S. R. Bare and E. Nikolla, *JACS Au*, 2021, **1**, 2224–2241.
45 C. W. Tung, Y. Y. Hsu, Y. P. Shen, Y. Zheng, T. S. Chan, H. S. Sheu, Y. C. Cheng and H. M. Chen, *Nat. Commun.*, 2015, **6**, 8106.
46 G. Ding, H. Lee, Z. Li, J. Du, L. Wang, D. Chen and L. Sun, *Adv. Energy Sustain. Res.*, 2022, **4**, 2200130.
47 W. Yan, Y. Mou, M. Li, K. Ma, Z. Xu, T. Lu, H. Du, C. Wang, H. Sun, L. Chen, Y. Tang, Y. Wang and G. Fu, *Adv. Mater.*, 2025, **37**, 2506936.
48 H. Zhang, H. Guo, F. Zhang, J. Zhang, Y. Cheng, Y. Ma, L. Ma and L. Qi, *Energy Environ. Sci.*, 2025, **18**, 6141–6153.
49 H. J. Niu, C. Huang, T. Sun, Z. Fang, X. Ke, R. Zhang, N. Ran, J. Wu, J. Liu and W. Zhou, *Angew. Chem., Int. Ed.*, 2024, **63**, e202401819.
50 K. Yassin, R. Attias, Y. Tsur and D. R. Dekel, *ACS Electrochem.*, 2025, **1**, 655–666.
51 L. Zeng, Z. Zhao, Q. Huang, C. Zhou, W. Chen, K. Wang, M. Li, F. Lin, H. Luo, Y. Gu, L. Li, S. Zhang, F. Lv, G. Lu, M. Luo and S. Guo, *J. Am. Chem. Soc.*, 2023, **145**, 21432–21441.
52 Y. Zhang, Q. Wan, L. Huang, T. Jiang, S. Wu, D. Li, Y. Liu, H. Wu and F. Ren, *J. Mater. Chem. A*, 2025, **13**, 17384–17392.
53 L. Guo, Y. Huang, Y. Qin, B. Chen, C. Liu, H. Chen, J. Zhang, X. Zhang and Q. Wang, *Nanoscale*, 2025, **17**, 17312–17323.
54 B. Ravel and M. Newville, *J. Synchrotron Radiat.*, 2005, **12**, 537–541.
55 P. K. Gangadharan, H. Kuroki, S. Miyanishi, H. Okuyama and T. Yamaguchi, *ACS Appl. Energy Mater.*, 2025, **8**, 10637–10646.
56 S. Narayanaru, H. Kuroki, T. Tamaki, G. M. Anilkumar and T. Yamaguchi, *RSC Sustain.*, 2025, **3**, 1705–1713.
57 K. Nagasawa, T. Ishida, H. Kashiwagi, Y. Sano and S. Mitsushima, *Int. J. Hydrogen Energy*, 2021, **46**, 36619–36628.